Decay of Streamwise Vorticity Downstream of a Three-Dimensional Protuberance

Clarence W. Kitchens Jr.,* Nathan Gerber,† Raymond Sedney,‡ and Joan M. Bartos§
U.S. Army Armament Research and Development Command, Aberdeen Proving Ground, Maryland

Streamwise vortices generated in boundary layers are known to persist for hundreds of boundary-layer thicknesses. This remarkable property is the main topic of this paper. The particular case of the flowfield generated by a three-dimensional protuberance immersed in a flat plate boundary layer is studied using numerical modeling. Experimental measurements in a downstream crossflow plane are used to construct initial data for a marching calculation using the boundary-layer and boundary-region approximations; the latter includes crossflow diffusion terms. The former fails to predict the flowfield, but results from the latter agree qualitatively with aspects of the flowfield determined from the measurements of Tani et al. and are also in fair quantitative agreement.

Nomenclature

f_0, F_2 = functions employed in formulation of initial plane data, Eq. (21)
k = height of cylindrical protuberance, = 0.25 cm in experiment
L = reference length for nondimensionalizing, = 1 cm
p = pressure, g/(cm s^2)
P = $p/(\rho u_\infty^2)$
Re = $\rho u_\infty L/\mu$ = Reynolds number, = 3467 in experiment
Re_k = $\rho u_\infty k/\mu$ = roughness Reynolds number, = 550 in experiment
Re_{x_k} = $\rho u_\infty x_k/\mu$, = 2.08×10^5 in experiment
s = twice the value of y at which $U = \frac{1}{2} \times (U_1 + U_2)$, Fig. 2a, cm
u, v, w = velocity components in the directions of x, y, and z, respectively, cm/s
u_∞ = freestream velocity, = 520 cm/s in experiment
U, V, W = u/u_∞, v/u_∞, $Re^{1/2} w/u_\infty$, respectively
U_1, U_2 = maximum and minimum values of U, respectively, Fig. 2a
U_B = Blasius flat plate boundary-layer velocity, Eq. (20)
U_T = U velocity function obtained by fitting Tani data, Eqs. (17) and (22)
x, y, z = rectangular coordinates: streamwise, spanwise, and normal to wall, respectively, Fig. 1, origin at leading edge of flat plate; cm
x_k = x coordinate of cylindrical protuberance, Fig. 1, = 60 cm in experiment
X, Y, Z = x/L, y/L, $Re^{1/2} z/L$, respectively
$\bar{X}$ = $(x - x_k)/k$
X_I = X coordinate of initial data plane, = 62.5 in experiment
β_T = function describing spanwise variation of V_I/U_I, obtained by fitting Tani data, Eqs. (18) and (22)
δ = boundary-layer thickness, Fig. 1, cm
$\Delta X, \Delta Y, \Delta Z$ = increments in X, Y, and Z in finite difference equations
ϵ = 0 for boundary layer, = 1 for boundary region, Eqs. (14), (15), and (23)
ζ_x = streamwise vorticity $(\partial W/\partial Y - \partial V/\partial Z)$
η = $Z/(2X_I)^{1/2}$, Eq. (19)
μ = viscosity of air, g/(cm s)
ν = kinematic viscosity of air, = 0.15 cm^2/s in experiment
ρ = density of air, g/cm^3

Subscripts

i, j, k = indexes identifying grid points, Eq. (25)
I = initial plane of data
k = front of cylindrical protuberance
T = Tani measurement
∞ = freestream

Superscript

m = designator of iteration level

I. Introduction

A PROTUBERANCE in a boundary layer whose height is of the order of the boundary-layer thickness would be expected to cause large changes in the neighboring flowfield. Experimentally, it has been found that significant perturbations in the flow are also induced downstream of the protuberance for hundreds of protuberance heights. As determined by flow visualization and supported by hot-wire measurements, these perturbations take the form of streamwise vortices or concentrations of streamwise vorticity. A theoretical model for this persistent effect does not exist; in this paper numerical modeling is employed.

There are other flowfields where the persistence of streamwise vorticity has been found. In wind tunnel experiments on flat plates, nonuniformities in screens far upstream of the plate have caused significant spanwise velocity components. Small nonuniformities on the leading edge of plates or on steps of bodies of revolution also induce persistent streamwise vortices. Such vortices are also formed in the boundary layer on the leeward side of a body of revolution at moderate angle of attack and can persist to the base; as angle of attack increases, the vortices are shed from the body.

Presented as Paper 82-0217 at the AIAA 20th Aerospace Sciences Meeting, Orlando, Fla., Jan. 11-14, 1982; submitted Jan. 22, 1982; revision received July 6, 1982. This paper is declared a work of the U.S. Government and therefore is in the public domain.

*Chief, Blast Dynamics Branch, Terminal Ballistics Division, Ballistic Research Laboratory. Associate Fellow AIAA.

†Research Aerospace Engineer, Launch and Flight Division, Ballistic Research Laboratory. Member AIAA.

‡Fluid Dynamics Research Scientist, Launch and Flight Division, Ballistic Research Laboratory. Associate Fellow AIAA.

§Mathematician, Launch and Flight Division, Ballistic Research Laboratory.

These vortices can influence the forces and moments on a projectile.

The persistence of streamwise vortices is found for both laminar and turbulent boundary layers. For the latter, spanwise nonuniformity in the transition process can induce them in addition to the mechanisms mentioned earlier. Streamwise vorticity may also be involved in large-scale structures in turbulent boundary layers. A matter of practical concern when streamwise vortices exist in turbulent boundary layers is that they increase the heat transfer.

The preceding ideas are discussed by Morkovin,[1] who also emphasizes the unsatisfactory state of the observations and theory for streamwise vortices. The main conclusions of the present work are also discussed.

To study the effect, the simplest situation is chosen in which streamwise vortices are found: flow behind a protuberance imbedded in a low-speed laminar boundary layer on a flat plate. Also, more experimental data are available for this case than any other; even so, it is not sufficient for our purposes. The objective of this work is to determine if numerical simulation of the flowfield will show the persistence and other features of the flowfield that are observed experimentally.

A schematic of the flowfield is shown in Fig. 1. Qualitatively, the same flowfield features are found over a wide range of conditions, regardless of whether the boundary layer is laminar or turbulent, or whether the external flow is high speed or low speed. Sedney[2] has surveyed the effects of small protuberances on boundary-layer flows; for additional details of the flowfield and references describing them, see Ref. 2. As sketched in Fig. 1, the boundary layer separates upstream of the protuberance, forming a horseshoe vortex which stretches around the obstacle. Spiral vortices rise up from the surface of the plate in the near wake, forming twin-vortex filaments which trail downstream. Smoke visualization studies in low-speed boundary layers show that the streamwise vortices produced by the interaction process can remain steady and distinct for more than a hundred protuberance heights downstream of the obstacle. The persistence of these vortices is quite remarkable, even more so when it occurs in turbulent boundary layers, considering the high diffusivity.

Two numerical approaches for modeling the downstream flowfield are employed in the present study: three-dimensional boundary-layer approximations and a three-dimensional boundary-region approximation which includes the viscous crossflow (diffusion) terms neglected in the boundary-layer theory. The measurements of Tani et al.,[3] taken ten protuberance heights downstream of the obstacle, are used to construct the initial data for the calculations. Quantitative agreement between the numerical simulation and measurements will depend on the accuracy with which we can fit the initial data, which are obtained from experimental measurements and properties of boundary layers. The uncertainties in the fitting will be described.

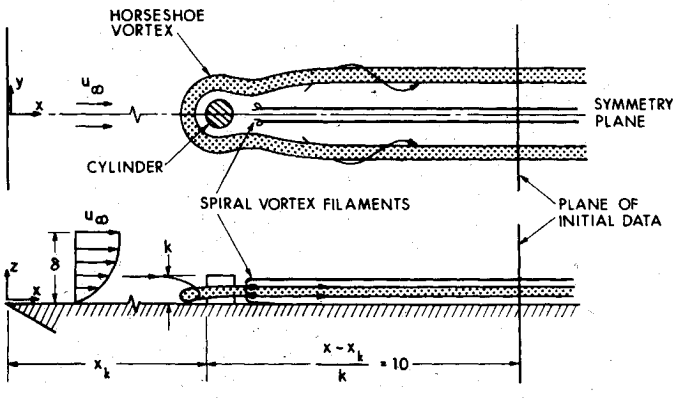

Fig. 1 Sketch of protuberance in boundary layer in Tani experiment ($k/\delta=0.39$, $Re_{x_k}=2.08\times10^5$, $Re_k=550$).

The major conclusion is that, using the boundary-region approximation, we are able to reproduce the qualitative features of the flowfield far downstream of the obstacle, including the persistence of streamwise vorticity; but we do not succeed using the three-dimensional boundary-layer approximation.

II. Governing Equations

For some range of the parameters involved, such as Reynolds number, protuberance dimensions, and geometry, the flow is sensibly steady; see Ref. 2. Therefore, we use the steady, three-dimensional, incompressible Navier-Stokes equations.

$$uu_x+vu_y+wu_z=-\rho^{-1}p_x+\nu(u_{xx}+u_{yy}+u_{zz}) \tag{1}$$

$$uv_x+vv_y+wv_z=-\rho^{-1}p_y+\nu(v_{xx}+v_{yy}+v_{zz}) \tag{2}$$

$$uw_x+vw_y+ww_z=-\rho^{-1}p_z+\nu(w_{xx}+w_{yy}+w_{zz}) \tag{3}$$

and the continuity equation

$$u_x+v_y+w_z=0 \tag{4}$$

where subscripts denote partial differentiation, ρ the density, p the pressure, ν the kinematic viscosity; and u,v,w are dimensional velocity components in the directions of the streamwise coordinate x, the spanwise coordinate y, and the normal to the plate z, respectively (see Fig. 1 for coordinate system). Equations (1-4) are sufficient for describing the complete protuberance flowfield, but would be very difficult to apply in practice because marching schemes cannot be used. If we concentrate, instead, on the flowfield "far enough" downstream of the protuberance, we can obtain an initial-value problem in two ways. The first is obtained using the conventional three-dimensional boundary-layer approximations. Since the data we shall use in the present problem for the initial values show large crossflow gradients, we shall also use a second approximation called the three-dimensional boundary-region equations. These equations are appropriate for flows with large crossflow gradients.

The three-dimensional boundary-layer equations can be derived from Eqs. (1-4) through either an order-of-magnitude analysis, or by formally applying limit processes at high Reynolds numbers. The resulting equations, in nondimensional form, are

$$UU_X+VU_Y+WU_Z=-P_X+U_{ZZ} \tag{5}$$

$$UV_X+VV_Y+WV_Z=-P_Y+V_{ZZ} \tag{6}$$

$$U_X+V_Y+W_Z=0 \tag{7}$$

where the nondimensional variables are defined by

$$X=x/L,\quad Y=y/L,\quad U=u/u_\infty,\quad V=v/u_\infty \tag{8}$$

$$Z=zRe^{1/2}/L,\quad W=wRe^{1/2}/u_\infty,\quad P=p/(\rho u_\infty^2) \tag{9}$$

with

$$Re=\rho u_\infty L/\mu \tag{10}$$

The freestream velocity is u_∞ and L represents a reference length, taken to be 1 cm in the present problem.

The three-dimensional boundary-region equations are

$$UU_X+VU_Y+WU_Z=-P_X+U_{ZZ}+Re^{-1}U_{YY} \tag{11}$$

$$UV_X+VV_Y+WV_Z=-P_Y+V_{ZZ}+Re^{-1}V_{YY} \tag{12}$$

$$U_X+V_Y+W_Z=0 \tag{13}$$

These equations cannot be formally derived from Eqs. (1-4), to the best of our knowledge. Rather, they represent an ad hoc approximation that has been used in some other investigations to treat problems where crossflow diffusion effects were not negligible. They were first used by Kemp[4] for the flow over two intersecting flat plates, the corner problem, and have been employed extensively by many authors for that problem. The boundary-region equations can be derived, using familiar limiting processes, for the corner problem, but not for the present problem or others to which they have been applied.

We can write a single set of equations that expresses both the boundary-layer and boundary-region approximations

$$UU_X + VU_Y + WU_Z = -P_X + \epsilon Re^{-1} U_{YY} + U_{ZZ} \tag{14}$$

$$UV_X + VV_Y + WV_Z = -P_Y + \epsilon Re^{-1} V_{YY} + V_{ZZ} \tag{15}$$

$$U_X + V_Y + W_Z = 0 \tag{16}$$

where $\epsilon = 0$ gives the three-dimensional boundary-layer equations and $\epsilon = 1$ gives the three-dimensional boundary-region equations. In each momentum equation the boundary-region approximation includes one additional crossflow diffusion term that is neglected in the three-dimensional boundary-layer theory. Both approximations neglect the normal momentum equation, assuming that the normal pressure gradient $P_Z = 0$. The boundary conditions applicable to Eqs. (14-16) will be described in Sec. V. When the external flow is uniform, as is assumed here, $P_X = P_Y = 0$.

III. Tani Test Problem

We have attempted to apply Eqs. (14-16) to describe the flowfield downstream of a typical small cylindrical protuberance. Experimental hot-wire anemometry measurements taken by Tani et al.[3] establish the presence and persistence of streamwise vortices in the downstream flowfield for various freestream conditions. The test problem treated here corresponds to Tani's experimental arrangement with a cylindrical protuberance ($k = 0.25$ cm), where k is the protuberance height, mounted normal to a flat plate placed in a wind tunnel; see Fig. 1. The protuberance height is equal to its diameter and the freestream velocity is 520 cm/s, with a freestream turbulence level of approximately 0.2%. The protuberance leading edge is located at $x_k = 60$ cm. For these conditions the protuberance height is approximately 39% of the local boundary-layer thickness δ, at $x = x_k$, based on the 99% velocity thickness. The Reynolds number based on x_k, with $\nu = \mu/\rho = 0.15$ cm^2/s is $Re_{x_k} = u_\infty x_k/\nu = 2.08 \times 10^5$ and the roughness Reynolds number is $Re_k = 550$, defined in terms of the protuberance height and the local undisturbed velocity at $x = x_k$, $z = k$.

Tani took hot-wire surveys of the protuberance flowfield at various x to study the manner in which the streamwise vortices redistribute momentum in the boundary layer and affect transition. His measurements taken at $\bar{X} = 10$, where $\bar{X} = (x - x_k)/k$ are used in the present study to construct a plane of data for "initializing" the marching schemes used to solve Eqs. (14-16). From the limited data taken by Tani, distributions of velocity components which fit these data must be constructed in order to generate the initial flow. This is accomplished by combining the available data with theoretical considerations, so that U, V, and W are prescribed everywhere at $\bar{X} = 10$. This process is described in the next section.

In addition to velocity fields, Ref. 3 presents data concerning the flow perturbation caused by the protuberance and the spacing of the vortices for $10 \le \bar{X} \le 244$; these data are used to test the calculations. The transition process, which starts at $x = x_t$, begins further downstream; from Ref. 3, $(x_t - x_k)/k \simeq 4500$.

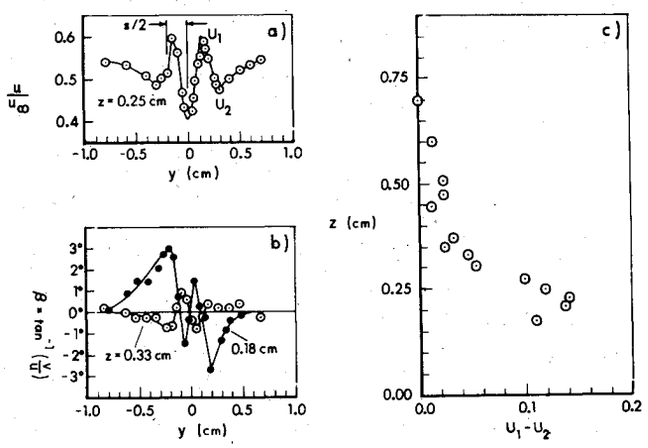

Fig. 2 Measured spanwise distribution at $\bar{X} = 10$ of a) streamwise velocity component and b) flow inclination in the x,y plane at two heights; c) experimental distribution across boundary layer of peak-valley velocity difference ($U_1 - U_2$) at $\bar{X} = 10$.

IV. Initial Plane of Data

The experimental data[3] shown in Fig. 2 are used to construct the velocities in the initial plane. The u and v distributions are consistent with two vortices, symmetrical about $y = 0$, but are insufficient to characterize the entire flowfield. They must be supplemented with theoretical considerations and assumptions. The deviation of the fitted values from the actual velocity field might be large for some y and z because of the paucity of the data.

Figures 2a and 2b furnish data at only three values of z, whereas values of $U_1 - U_2$ are given in Fig. 2c for many z values. The curves in these figures are from Ref. 3, representing the authors' smoothing of the data. Figure 2c, together with Fig. 6 of Ref. 3, shows that the shape of the $U(Y)$ curves is the same for all Z; only the magnitude changes. Three quantities are defined graphically in Fig. 2a: U_1 and U_2 are the maximum and minimum values, respectively, of U off the plane of symmetry at fixed values of Z; $s/2$ is the maximum value of Y at which $U = \frac{1}{2} \times (U_1 + U_2)$ and is, thus, a measure of the spacing of the two legs of the horseshoe vortex. A measure of the perturbation due to the horseshoe vortex is $U_1 - U_2$; for Fig. 2 it is approximately 20% of the local Blasius value of U.

The fits for U and V in the initial plane are

$$U_I = U_B + 1.961\,[1.519\eta f_0''(1.519\eta)]\,[U_T(Y) - U_T(2.5)] \tag{17}$$

$$V_I = -1.217\eta U_I F_2(1.558\eta) \tan\beta_T(Y) \tag{18}$$

where

$$\eta = Z/(2X_I)^{1/2} = [u_\infty/(2\nu x_I)^{1/2}]\,z \tag{19}$$

$$U_B = f_0'(\eta) \tag{20}$$

are the Blasius variables. The process which led to these fitting functions is described next.

The functions $f_0'(\eta)$, $\eta f_0''(\eta)$, and $F_2(\eta)$ are tabulated in Appendix A of Ref. 5. These are obtained by solving

$$f_0'''(\eta) + f_0 f_0'' = 0 \qquad F_2'' + f_0 F_2' + 3.3873 f_0' F_2 = 0 \tag{21}$$

where

$$f_0(0) = f_0'(0) = 0 \qquad f_0'(\infty) = 1 \qquad F_2(0) = F_2(\infty) = 0$$

F_2 is an eigenfunction occurring in the boundary-layer perturbation analysis of Fox and Libby.[6]

The functions $U_T(Y)$ and $\beta_T(Y)$ are obtained by dividing the Y axis into segments and empirically fitting the data of

Fig. 2 in each segment with a third-order polynomial, with continuity of the functions and first derivatives required at tie points.

$$U_T(Y) = a_0 + a_1 Y + a_2 Y^2 + a_3 Y^3$$
$$\beta_T(Y) = b_0 + b_1 Y + b_2 Y^2 + b_3 Y^3 \text{ (deg)} \tag{22}$$

where β_T is fitted at $z=0.18$ cm. The imposed symmetry requires that we need to consider only $Y \geq 0$. Five segments were used here. The a_j and b_j coefficients and tie points are provided in Appendix B of Ref. 5. Regrettably, the boundary-region approximation was not under consideration when the cubic spline fits were made for U_T and β_T; consequently, U_{YY} and V_{YY} in Eqs. (14) and (15) are discontinuous at the tie-points.

The following process was used to arrive at Eqs. (17) and (18). We imposed the plausible assumption that as either $Y \to \infty$ or $Z \to \infty$, U approaches Blasius flow and V approaches zero. In Eq. (17) the Blasius U is reached at $Y=2.5$. The function $\eta f_0''(\eta)$ has the same shape and limits as the $U_1 - U_2$ data in Fig. 2c, which measure the amplitude of perturbation to Blasius flow. The two constants in Eq. (17) were obtained by imposing two conditions: 1) U should agree with Tani's measurement at $y=0.30$ cm and $z=0.25$ cm (Fig. 2a), and 2) the peak of the $\eta f_0''(\eta)$ curve should occur at $z=0.24$ cm, the peak of the data in Fig. 2c. As for Eq. (18), Fig. 2b indicates a reversal in phase of the β vs y profiles between $z=0.18$ cm and $z=0.33$ cm; the function $F_2(\eta)$ provides this feature. The two constants in Eq. (18) were obtained by forcing the analytical expression for V_1 to agree with the data at $y=0.30$ cm, $z=0.18$ cm, and $y=0.30$ cm, $z=0.33$ cm.

Results of the fitting are compared with Tani's measurements in Fig. 3, which shows spanwise distributions for both $y<0$ and $y>0$, and Fig. 4, which shows variation normal to the plate. In Fig. 3b only the data for $y>0$ and $z=0.18$ cm were used to determine the constants, and the deviation between these data and the fitted curve is relatively small. Although the deviation for $y<0$ is relatively large, it is apparent that the scatter in the data is also large, e.g., the data for β is not an odd function of y. In fitting the data, however, we required the symmetry conditions to be satisfied.

The vertical component W is found from U and V by subtracting Eq. (14) from [U times Eq. (16)], then separating out the resulting $\partial(W/U)/\partial Z$ term and integrating

$$W = U\int_0^Z \{[P_X - UV_Y + VU_Y - (\epsilon Re^{-1}U_{YY} + U_{ZZ})]/U^2\}\,dZ \tag{23}$$

A similar expression can be derived using Eqs. (15) and (16). For uniform external flow, $P_x=0$. The Y and Z derivatives are evaluated by finite differences at the mesh points in the Y,Z plane with three-point formulas, and W is obtained by numerical integration of the right-hand side of Eq. (23). The integrand J of Eq. (23) is indeterminate but finite at $Z=0$, so that at the first level of mesh points off the plate,

$$W(Z=\Delta Z) = U(\Delta Z)J(\Delta Z/2)\Delta Z/2$$

The computation fails if $U=0$ off the plate; however, this has never occurred. The boundary-layer and boundary-region approximations yield different distributions because of the absence or presence of the $Re^{-1}U_{YY}$ term.

In Fig. 5 the velocity vectors are shown projected into the initial plane (as viewed looking downstream from the protuberance). The U and V components are identical in both approximations, but the W components are different. A mesh point lies at the tail of each velocity vector. The boundary-layer approximation leads to two counter-rotating vortices on each side of the plane of symmetry. In the boundary-region

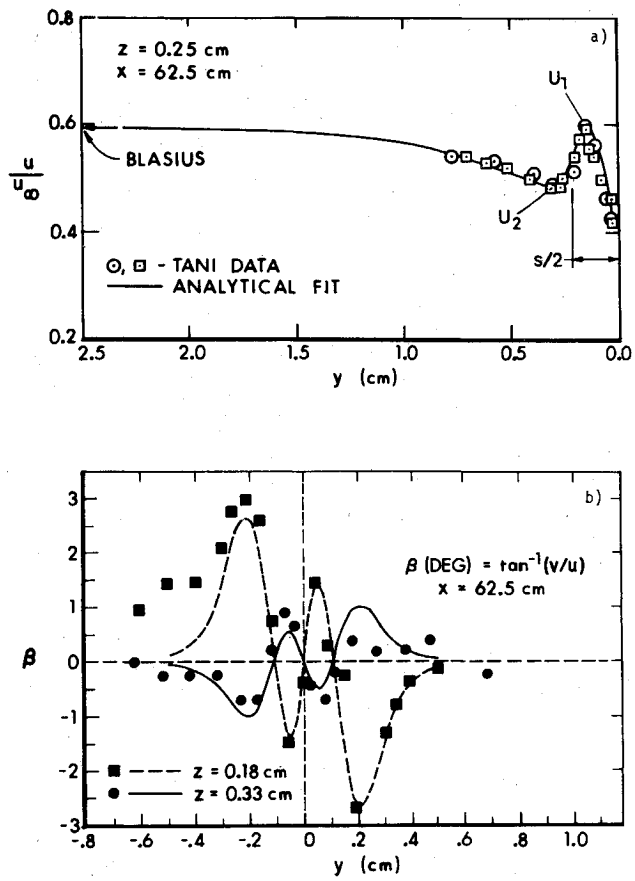

Fig. 3 Analytical spanwise distributions of a) u/u_∞ and b) $\beta \equiv \tan^{-1}(v/u)$, Eqs. (17) and (18), at fixed heights in the initial data plane, and comparison with Tani data.

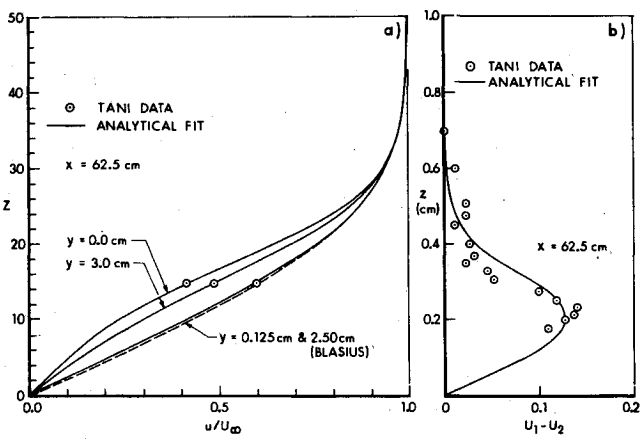

Fig. 4 Analytical distributions of a) u/u_∞ and b) $U_1 - U_2$ through the boundary layer in the initial data plane, and comparison with Tani data.

approximation, there is one large vortex and possibly several smaller vortices that are not clearly defined. One noticeable difference occurs at the plane of symmetry, $Y=0$; in the boundary-region case the flow is toward the plate, while in the boundary-layer case the flow is away from the plate.

The differences between the two flow patterns in Fig. 5 suggest that U_{YY}, and, therefore, V_{YY} are not negligible for this vortical flow. Figure 6 compares u_{yy} with u_{zz} at $Z=1.0$. (Since these two terms are dimensional, they may be compared directly, no stretching factor being involved.) This figure shows that u_{yy} is eight times as large as u_{zz} in some parts of the initial plane. Thus the boundary-layer ap-

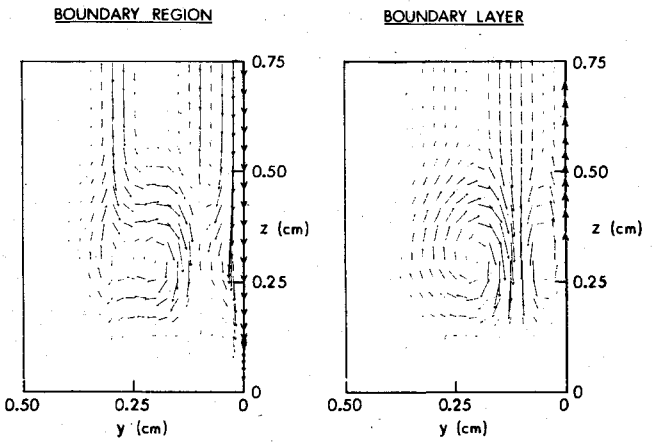

Fig. 5 Crossflow plane (y,z) velocity vector projections in initial data plane at $\bar{X}=10$.

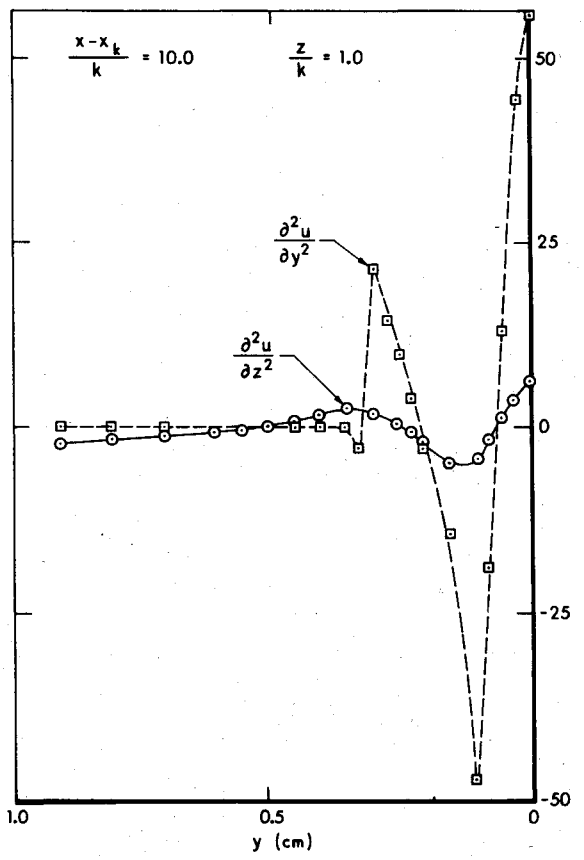

Fig. 6 Spanwise distribution of second derivatives of streamwise velocity component at $\bar{X}=10$.

proximation is violated in this plane because it requires $u_{yy} \ll u_{zz}$.

That the boundary-layer approximation may be violated can be anticipated from the large gradients, e.g., U_y shown in the data in Fig. 2a. The question arises whether or not a boundary-layer calculation should be attempted. It was decided to do this on the possibility that the large gradients would be smoothed out and that the downstream flow could be calculated.

V. Numerical Procedure and Boundary Conditions

The equations were solved using the predictor-corrector multiple-iteration (PCMI) method, which has two advantages. It can be used for both sets of equations, and the truncation error is uniformly second order. One alternative procedure for the boundary-layer equations is discussed later.

The numerical solution to Eqs. (14-16) is obtained by marching downstream (X direction) from the initial data plane. Symmetry boundary conditions

$$\frac{\partial U}{\partial Y} = V = \frac{\partial W}{\partial Y} = 0 \tag{24}$$

are applied at $Y=0$ and Blasius flow is prescribed at $Y=2.5$. The freestream velocity components ($U=1$ and $V=0$) are prescribed at $Z=100$. The numerical procedure is based on the PCMI technique developed by Rubin and Lin.[7] The procedure is implicit in the Z direction. All flow gradients in the Y direction are approximated by prediction and subsequent correction using an iterative approach, which gives a more accurate simulation of the nonlinear coupling between equations. The solution is obtained for each grid column by inverting a tridiagonal matrix.

The complete set of difference equations used in this study is given in Appendix C of Ref. 5. The truncation errors for interior points are of $\mathcal{O}(\Delta X^2, \Delta Y^2, \Delta Z^2)$. The PCMI procedure solves the momentum difference equations for U^{m+1} and V^{m+1}, using the mth iterate values to form the coefficients of the nonlinear terms and approximate Y derivatives, where m denotes the iteration level. The continuity equation is then solved for W^{m+1}.

For the predictor step, or first iteration, a Taylor series to $\mathcal{O}(\Delta X^2)$ is used.

$$F^0_{i+1,j,k} = F_{i,j,k} + (F_{i,j,k} - F_{i-1,j,k})\,(X_{i+1} - X_i)\,/\,(X_i - X_{i-1}) \tag{25}$$

During the first X step an extrapolation of $\mathcal{O}(\Delta X)$ is used. After extrapolating guesses for U^0, V^0, and W^0 at X_{i+1}, difference equations (see Ref. 5) are solved to give U^1 and V^1. The calculations start at the plane of symmetry and work outward in Y. The $(m+1)$-th iterate values are used to approximate derivatives in the Y direction as soon as they become available. Next W^1 is obtained, starting at $Y=Z=0$ and sweeping in Z and then Y. This completes the first iteration cycle. Subsequent iterations allow the nonlinear terms to be corrected and the symmetry plane boundary conditions to be satisfied.

Numerical studies were performed to determine the number of iterations required to give satisfactory convergence of the solution. These indicate that three iterations assure convergence of U, V, and W to at least four decimal places, which we consider to be sufficiently accurate. Consequently, at least three iterations were used for subsequent calculations. The number of iterations used varied with ΔX, which ranged from 0.010 near the initial data plane to 0.250 at the last downstream station. The value of ΔX was adjusted during the calculations to satisfy the linear stability criterion

$$\Delta X \le \Delta Y\,|U/V| \tag{26}$$

Equation (26) is based on a linear stability analysis for interior points, including the effect of multiple iteration.[7] A 41×41 ($Y \times Z$) grid was used for each $X=$const plane with $\Delta Y=0.025$ for $0 \le Y \le 0.5$, $\Delta Y=0.100$ for $0.5 < Y \le 2.5$ and $\Delta Z=2.50$ for $0 \le Z \le 100$. The variable spacing in Y was adopted to help resolve the large crossflow gradients indicated in Fig. 2 for $0 \le Y \le 0.5$. Special second-order accurate difference approximations for $\partial F/\partial Y$ and $\partial^2 F/\partial Y^2$ are employed at $Y=0.5$ due to the unequal mesh spacing, where F represents U or V.

VI. Results and Comparison with Experiment

Computations were carried out for the vortical flow downstream of the protuberance using both the boundary-layer and boundary-region approximations. The boundary-layer calculation failed when it predicted streamwise flow

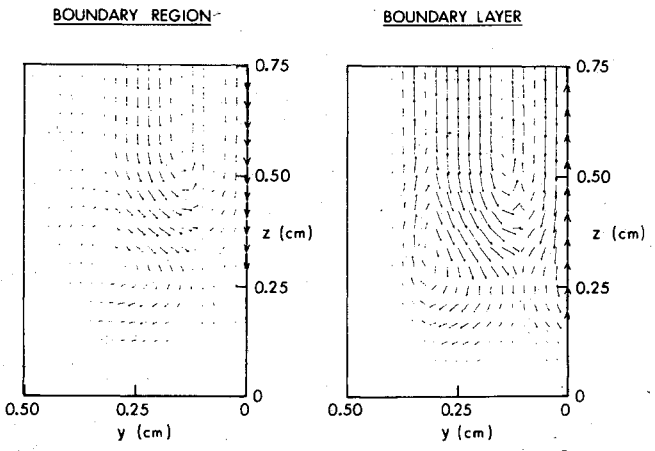

Fig. 7 Crossflow plane (y,z) velocity vector projections at $\bar{X}=16$.

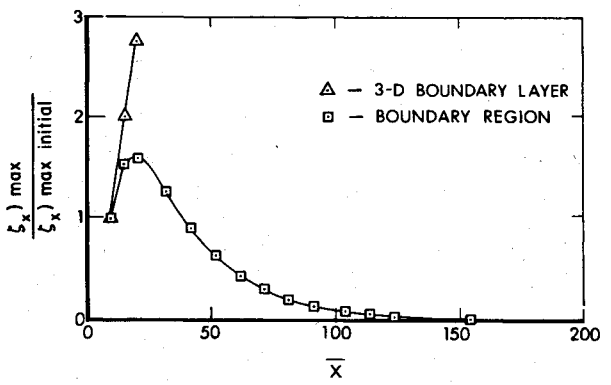

Fig. 8 Streamwise variation of maximum vorticity at wall.

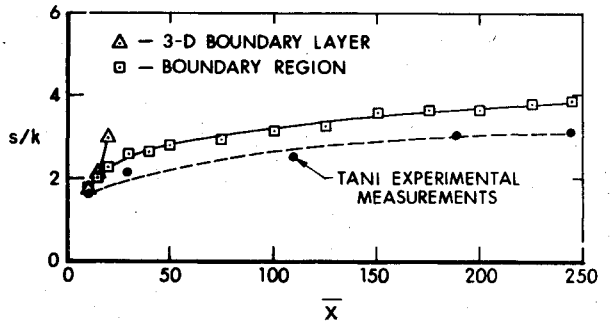

Fig. 9 Streamwise variation of horseshoe vortex spacing.

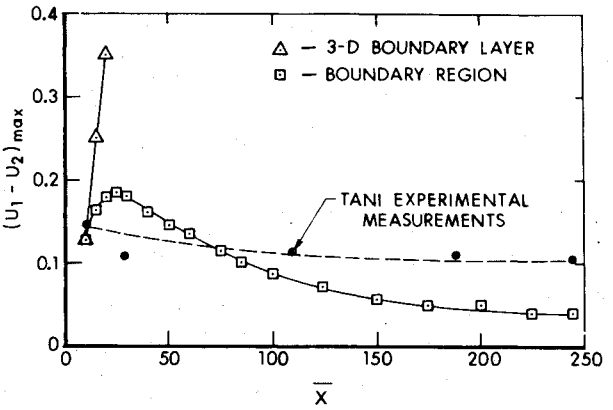

Fig. 10 Streamwise variation of maximum peak-valley velocity difference induced by horseshoe vortex.

reversal; the boundary-region calculation, on the other hand, was carried to 244 protuberance heights downstream (Tani's last station) without encountering computational difficulties.

Crossflow velocity vector plots at $\bar{X}=16$ are presented in Fig. 7, which shows the initial stages of the breakdown of the boundary-layer calculation. Large gradients, W_Y, are predicted at $Y=0.025$ and 0.3 which were not present in the initial plane. As the calculation proceeds, they are not smoothed out, due to lack of crossflow diffusion. The positive W along the plane of symmetry, present on the initial plane, is still in evidence. At $\bar{X}=20$ the W component is larger and the U component reverses direction, as if streamwise separation had occurred. Since there is no pressure gradient in this flow, the usual cause of separation, an adverse pressure gradient, cannot be invoked. We only note that 1) for both the initial plane and for $\bar{X}=16$, $W>0$ in the neighborhood of $Y=0$, and 2) $U_Z>0$ up to the point of flow reversal; thus, the term WU_Z could play the role of an adverse pressure gradient. At any rate the boundary-layer calculation cannot proceed beyond $\bar{X}=20$.

For the boundary-region calculation the crossflow velocity vector plot in Fig. 7 shows that some anomalies that existed in the initial plane, caused by discontinuities in second derivatives with respect to Y, have been smoothed out. The presence of the main vortex is clearly seen. In contrast to the boundary-layer results, $W<0$ near $Y=0$, as it was in the initial plane, and the gradients are smaller; the largest W_Y for the boundary-region case being 20% of that for the boundary-layer case.

Figure 8 shows the downstream variation of the maximum value of the streamwise vorticity, ζ_x $(=\partial W/\partial Y-\partial V/\partial Z)$, evaluated at the wall. This can be used as an indicator of the strength of the horseshoe vortex. Results from the boundary-layer calculation are terminated where it breaks down. The streamwise vorticity from the boundary-region calculation is essentially zero at about 150 protuberance heights downstream.

With regard to crossflow velocity, the boundary-region calculation predicts that the flow inclination at $\bar{X}=244$ is less than 0.2 deg. Tani could not detect any crossflow velocity component at 244 protuberance heights downstream. In fact, 0.2 deg is within scatter of this data.

Figure 9 shows the streamwise variation of the horseshoe vortex spacing s. The variation predicted by the boundary-region approximation is seen to agree qualitatively with Tani's measurements. At the last downstream station the predicted spacing is about 25% larger than the measurement. The trend of calculated s is the same as that of the data.

Figure 10 shows the variation of the maximum velocity difference $(U_1-U_2)_{max}$. The quantity U_1-U_2 is evaluated in each crossflow plane and the largest value $(U_1-U_2)_{max}$ is plotted. The boundary-region calculation predicts that the perturbation in U grows to ~ 0.19 at $\bar{X}=25$ and then begins to decay. The calculated perturbation decays faster than the measured value up to $\bar{X}=200$; thereafter, the calculated value is essentially constant and is 38% of the experimental value at 244 protuberance heights downstream. Note that the perturbation in U is still present at $\bar{X}=244$, although the crossflow velocity has decayed to nearly zero and the maximum streamwise vorticity at the wall is already zero. These conclusions apply also to the experimental data.

The failure of the boundary-layer calculation would seem to be related to the lack of a mechanism for smoothing out or diffusing the large crossflow gradients in the initial data. However, care must be taken in drawing conclusions from the results of these numerical solutions because the failure of the PCMI boundary-layer calculation may be a product of the numerical scheme itself. An indication might be obtained by trying other schemes. Rather than try schemes similar to the PCMI, which would probably fail in the same way, we used a quite different scheme that gives results that appear to add support to the statement made in the first sentence of this paragraph. The scheme was the one in Ref. 8, called scheme

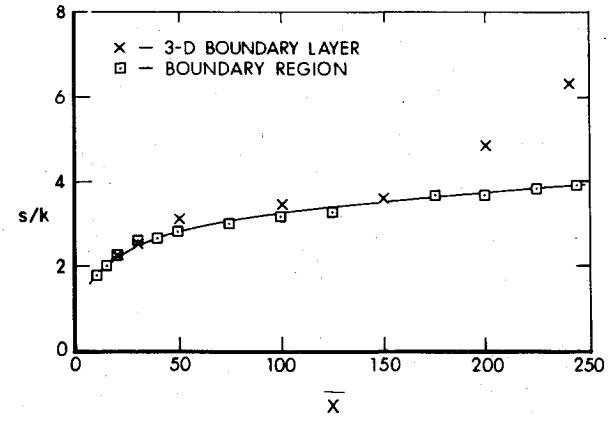

Fig. 11 Comparison of horseshoe vortex spacing: boundary region vs three-dimensional boundary layer (scheme D).

D, and was chosen on the basis of zone-of-dependence sensitivity; for details see Ref. 8. The truncation errors for this scheme are $\mathcal{O}(\Delta X, \Delta Y^2, \Delta Z^2, \Delta Y^2/\Delta X)$. In contrast with the PCMI truncation error, this scheme is only first order in ΔX and has the additional error $\Delta Y^2/\Delta X$. The latter arises from artificial diffusion introduced by the X difference equation. Using standard truncation error analysis techniques, it can be shown that two artificial viscosity terms, αU_{YY} and αV_{YY}, where $\alpha = \Delta Y^2/\Delta X$, are introduced into the finite difference equations.[9] These two artificial viscosity terms have the same form as the crossflow diffusion terms in the boundary-region approximation. These terms have the effect of smoothing out the initial large crossflow gradients, and the calculation proceeds beyond the point where the boundary-layer PCMI calculation failed. Apparently the scheme D boundary-layer difference equations behave in a manner similar to the boundary-region approximation. By increasing ΔX from 0.01 at the initial plane to 0.50 far downstream, the calculation proceeded to $\bar{X} = 244$. However, the results compared poorly with the data. Figure 11 shows the values of s from this scheme together with the boundary-region result. The divergence between the results, as X increases, may be caused by the fact that α is 50 times smaller downstream than near the initial plane, and, hence, the artificial diffusion is small, or perhaps because ΔX is 50 times larger than near the initial plane and, thus, produces unacceptable truncation errors. The conclusion is that this boundary-layer calculation fails but in a different sense from the PCMI failure.

VII. Conclusions

In this study we have shown that the three-dimensional boundary-region approximation can be used successfully to describe the flow downstream of a cylindrical protuberance immersed in a laminar flat plate boundary layer. The persistence of the streamwise vorticity downstream of the obstacle is predicted in agreement with experimental observations. We find that the streamwise vorticity persists more than 100 protuberance heights downstream and that the initial perturbations in U decay more slowly than the vorticity. Significant perturbations in U are still present 244 protuberance heights downstream of the obstacle in the boundary-region calculation. This is quite remarkable considering that we have marched more than one hundred boundary-layer thicknesses downstream to reach this position. The experimental data show the same qualitative trend.

The three-dimensional boundary-layer approximation, on the other hand, is not successful in describing the flowfield downstream of the protuberance. It fails due to the large crossflow gradients present in the protuberance flowfield. These gradients lead to the reversal of the streamwise velocity component U during the marching process.

It is expected that the quantitative agreement between the boundary-region calculations and Tani's experimental data would be improved if the initial data were fitted using fourth-order (or higher) polynomials so that U_{YY} and V_{YY} were continuous. Accuracy could be further improved by using smaller grid sizes during the marching process. Unfortunately, it is not possible to quantify the expected improvement. These refinements may not be warranted in the present problem, considering the sparse experimental data available for constructing initial data.

Whether or not the boundary-region approximation employed here is the most adequate model for this flowfield cannot be established unequivocably by this investigation. In our version we assumed that the normal pressure gradient, $\partial P/\partial Z$, is zero. It is possible that dropping this assumption would improve the quantitative agreement with experiment.

References

[1] Morkovin, M. V., "Observations on Streamwise Vortices in Laminar and Turbulent Boundary Layers," NASA CR 159061, April 1979.

[2] Sedney, R., "A Survey of the Effects of Small Protuberances on Boundary-Layer Flows," *AIAA Journal,* Vol. 11, June 1973, pp.782-792.

[3] Tani, I., Komoda, H., and Komatsu, Y., "Boundary-Layer Transition by Isolated Roughness," Aeronautical Research Institute Rept. 375, University of Tokyo, Nov. 1962.

[4] Kemp, N., "The Laminar Three-Dimensional Boundary Layer and a Study of the Flow Past a Side Edge," Masters of Aeronautical Science Thesis, Cornell University, 1951.

[5] Kitchens, C. W. Jr., Gerber, N., Sedney, R., and Bartos, J. M., "Streamwise Vorticity Decay Downstream of a Three-Dimensional Protuberance," U.S. Army Ballistic Research Laboratory, Tech. Rept. ARBRL-TR-02375, Aberdeen Proving Ground, Md., Oct. 1981, AD A108080.

[6] Fox, H. and Libby, P. A., "Some Perturbation Solutions in Laminar Boundary Layer Theory. Part 2. The Energy Equation," *Journal of Fluid Mechanics,* Vol. 19, July 1964, pp. 433-451.

[7] Rubin, S. G. and Lin, T. C., "A Numerical Method for Three-Dimensional Viscous Flow: Application to the Hypersonic Leading Edge," *Journal of Computational Physics,* Vol. 9, April 1972, pp. 339-364.

[8] Kitchens, C. W. Jr, Sedney, R., and Gerber, N., "The Role of the Zone of Dependence Concept in Three-Dimensional Boundary-Layer Calculations," U.S. Army Ballistic Research Laboratory/ARRADCOM Rept. 1821, Aberdeen Proving Ground, Md., Aug. 1975, AD A016896.

[9] Roache, P. J., "On Artificial Viscosity," *Journal of Computational Physics,* Vol. 10, Oct. 1972, pp. 169-184.